



Developing physics basis for the snowflake divertor in the DIII-D tokamak

V.A. Soukhanovskii¹ , S.L. Allen¹, M.E. Fenstermacher¹, C.J. Lasnier¹, M.A. Makowski¹, A.G. McLean¹, W.H. Meyer¹, D.D. Ryutov¹, E. Kolemen², R.J. Groebner³, A.W. Hyatt³, A.W. Leonard³ , T.H. Osborne³, T.W. Petrie³ and J. Watkins⁴

¹ Lawrence Livermore National Laboratory, 7000 East Ave, Livermore, CA 94550, United States of America

² Princeton University, Princeton, NJ 08540, United States of America

³ General Atomics, PO Box 85608, San Diego, CA 92186, United States of America

⁴ Sandia National Laboratories, PO Box 969 Livermore, CA 94551, United States of America

E-mail: vlad@llnl.gov

Received 20 September 2017, revised 27 December 2017

Accepted for publication 9 January 2018

Published 1 February 2018



Abstract

Recent DIII-D results demonstrate that the snowflake (SF) divertor geometry (see standard divertor) enables significant manipulation of divertor heat transport for heat spreading and reduction in attached and radiative divertor regimes, between and during edge localized modes (ELMs), while maintaining good H-mode confinement. Snowflake divertor configurations have been realized in the DIII-D tokamak for several seconds in H-mode discharges with heating power $P_{\text{NBI}} \leq 4\text{--}5$ MW and a range of plasma currents $I_p = 0.8\text{--}1.2$ MA. In this work, inter-ELM transport and radiative SF divertor properties are studied. Significant impact of geometric properties on SOL and divertor plasma parameters, including increased poloidal magnetic flux expansion, divertor magnetic field line length and divertor volume, is confirmed. In the SF-minus configuration, heat deposition is affected by the geometry, and peak divertor heat fluxes are significantly reduced. In the SF-plus and near-exact SF configurations, divertor peak heat flux reduction and outer strike point heat flux profile broadening are observed. Inter-ELM sharing of power and particle fluxes between the main and additional snowflake divertor strike points has been demonstrated. The additional strike points typically receive up to 10–15% of total outer divertor power. Measurements of electron pressure and poloidal beta β_p support the theoretically proposed churning mode that is driven by toroidal curvature and vertical pressure gradient in the weak poloidal field region. A comparison of the 4–4.5 MW NBI-heated H-mode plasmas with radiative SF divertor and the standard radiative divertor (both induced with additional gas puffing) shows a nearly complete power detachment and broader divertor radiated power distribution in the SF, as compared to a partial detachment and peaked localized radiation in the standard divertor. However, insignificant difference in the detachment onset w.r.t. density between the SF and the standard divertor was found. The results complement the initial SF divertor studies conducted in high-power H-mode discharges in the NSTX and DIII-D tokamaks, and, along with snowflake divertor results from TCV and other tokamaks, contribute to the physics basis of the SF divertor as a power exhaust concept for future high power density tokamaks.

Keywords: snowflake divertor, divertor, DIII-D, divertor detachment

(Some figures may appear in colour only in the online journal)

1. Introduction

Based on nearly five decades of magnetically confined nuclear fusion plasma physics research, an axisymmetric magnetic X-point divertor is envisioned as the plasma-material interface for the tokamak-based reactor. Intense heat and particle fluxes from the core plasma escape to the scrape-off layer (SOL) region and follow open field lines to a separate divertor chamber for mitigation and control of heat loads and material erosion. The steady-state mitigation techniques include partitioning the power that flows into the SOL (P_{SOL}) between divertor targets, reducing parallel heat and particle fluxes via volumetric losses and radial spreading, and reducing the heat flux deposited on the plasma facing components (PFCs) via increasing the plasma-wetted area [1, 2]. However, for future tokamaks, e.g. the fusion nuclear science facilities (FNSF) [3, 4] and, ultimately, the DEMO [5], the standard radiative divertor may be insufficient to keep steady-state heat fluxes within the present technological limit of $5\text{--}10\text{ MW m}^{-2}$ and control erosion via reduced T_e simultaneously. Additionally, transient divertor heat fluxes from edge localized modes (ELMs) must be mitigated via ELM size reduction and peak heat flux reduction to the transient limit of $0.1\text{--}0.5\text{ MJ m}^{-2}$. It is envisioned that an advanced magnetic configuration divertor optimized for heat and particle flux mitigation would take advantage of a combination of techniques, e.g. the magnetic geometry, plasma-facing component (PFC) geometry and structure, and impurity-seeded radiative solutions. Motivated by promising experimental and modeling results to date, a number of combined radiative and advanced divertor solutions have been proposed (as recently reviewed in, e.g. [6]).

A snowflake (SF) divertor magnetic configuration [7] has been proposed as a potential solution for the tokamak divertor power exhaust problem. The SF magnetic configuration includes a second-order poloidal field B_p null or two first-order nulls separated by a small distance [7–11]. Poloidal magnetic flux surfaces in the region of the exact second-order null have six separatrix branches with an appearance of a snowflake. The poloidal field B_p is a quadratic function of the distance from the null in the SF divertor (see linear in the standard divertor) [7], making the region of low B_p surrounding the null(s) broader. This property was theoretically predicted to have a strong impact on the pedestal and divertor plasma properties [10–13].

Encouraging results have been obtained in snowflake divertor experiments performed in the TCV [14–16], NSTX [17–20], DIII-D [20–23] tokamaks and two-null quasi-snowflake divertor experiments in EAST [24]. In TCV, ohmic and RF-heated H-mode plasmas, divertor heat flux sharing between multiple SF strike points was observed during ELMs and attributed to enhanced SOL transport. Initial experiments in DIII-D and NSTX using H-mode discharges with high divertor power densities demonstrated compatibility with high performance operation (as indicated by, e.g. the H-mode confinement factor $H_{98}(y,2) \geq 1$), modification of pedestal stability (in NSTX), significantly reduced inter-ELM and ELM

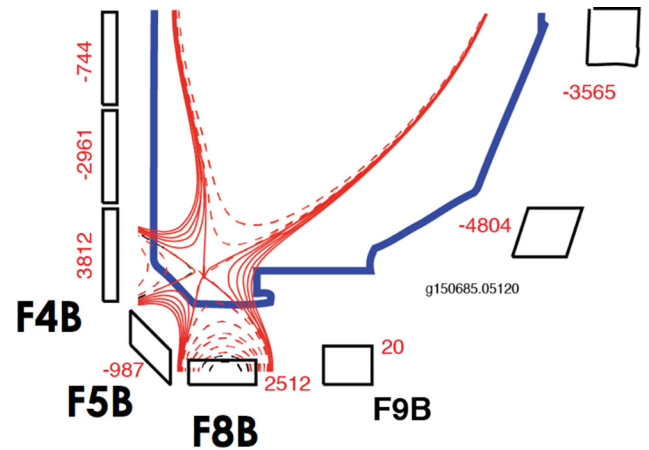


Figure 1. A layout of poloidal magnetic field coils in DIII-D tokamak. The coils F4B, F5B, and F8B are used for the SF divertor configurations. The coil currents used are expressed in Amps next to the coil schematics.

divertor heat flux, and facilitated access to partial strike point detachment (in NSTX).

In this paper we summarize the SF divertor properties obtained in DIII-D and report recent experiments that demonstrated heat transport modification and heat flux spreading in the attached divertor, and at the partially detached (radiative) divertor conditions between ELMs in the SF configuration, in comparison with the standard divertor. The paper is organized as follows. Experimental conditions are summarized in section 2. Snowflake divertor experimental results are presented in section 3, including geometric properties, divertor inter-ELM heat fluxes, particle and heat flux sharing between additional strike points, divertor poloidal β_p measurements and relation to the churning mode hypothesis, increased SOL power width, and radiative SF divertor properties. Section 4 contains discussion of the above results and conclusions.

2. Experiment

The SF divertor experiments were conducted in DIII-D using a standard highly-shaped lower single null H-mode discharge scenario with $B_t \leq 2\text{ T}$, $I_p = 0.8\text{--}1.2\text{ MA}$, $P_{\text{NBI}} \leq 5\text{ MW}$, and ion $B \times \nabla B$ drift toward the lower divertor. The DIII-D tokamak divertor is an open geometry divertor with graphite PFCs. In steady-state density scans, a divertor cryo-pump was used for particle removal, and D_2 seeding at a midplane location was used for average density \bar{n}_e variations in the range $\sim 4.5\text{--}7.5 \times 10^{19}\text{ m}^{-3}$ ($(0.4\text{--}0.7) \times n_e/n_G$, where n_G is the Greenwald density [25]). The DIII-D tokamak is equipped with a powerful core, edge and divertor diagnostic system. The divertor diagnostics used in this study included infrared thermography, Langmuir probes, divertor bolometry and divertor spectroscopy. Magnetic reconstructions were based on standard Grad–Shafranov equilibria reconstructed using the EFIT code.

The SF configurations were obtained using three existing poloidal field shaping coils F4B, F5B, and F8B in the lower divertor region, with currents $I \leq 5\text{ kA}$, as shown in figure 1.

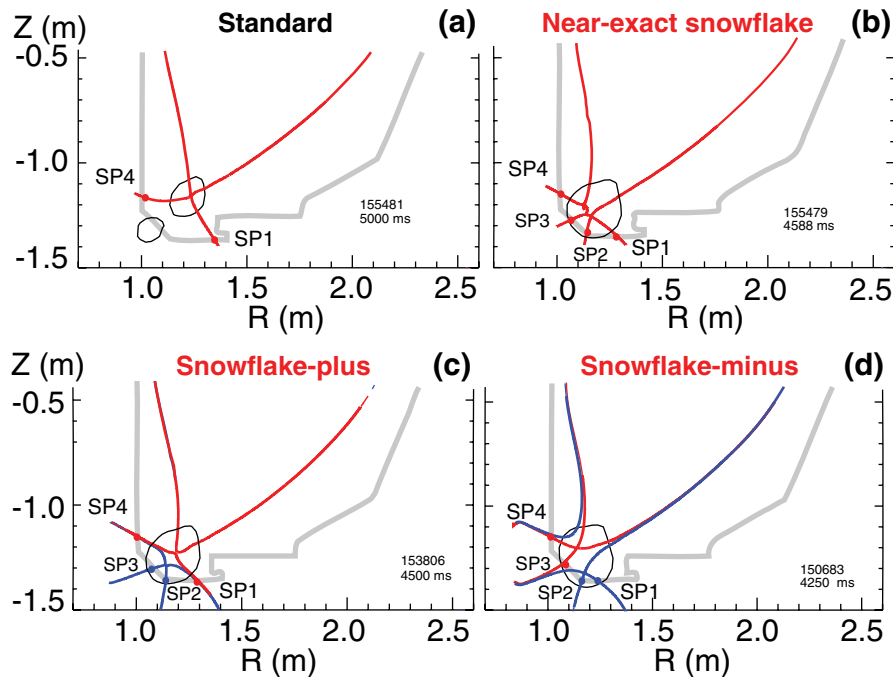


Figure 2. Typical magnetic equilibria of the standard (a), near-exact SF (b), SF-plus (c), and SF-minus (d) divertor configurations obtained in the experiment. The primary separatrices (red lines) and the secondary separatrices (blue lines) are shown. In the near-exact SF, the nulls either overlap or slightly move with respect to each other, so that SF-plus and SF-minus with a small time-varying $D \leq 0-5$ cm are realized. The line surrounding the null(s) region shows the extent of the low poloidal field region $B_p \leq 0.1 B_{pm}$, where B_{pm} is the outer midplane B_p .

The exact SF configuration with a second-order null is topologically unstable [7]: small variations of coil currents may lead to the break-up of the second order null into two physically separated first-order nulls. The two variants of the SF configuration often realized in steady-state experiments are called snowflake-plus (SF-plus) and snowflake-minus (SF-minus), as shown in figure 2. In the SF-plus, the secondary null is on the private flux region side of the standard divertor X-point. In the SF-minus, the secondary null is in the common flux SOL region. For SF-minus configurations, a combination of pre-programmed and real-time controlled coil currents (as in [18]) was used: the F4B and F8B coils were used for real-time strike point position control using the plasma control system (PCS), while F5B with a pre-programmed negative current was used for SF inter-null distance control. The coil F9B was disengaged (with $I_{F9B} \sim 0$ A) to avoid penetration of magnetic field lines under the divertor shelf to the regions unprotected by PFCs. The near-exact SF and SF-plus configurations were realized during SF control development experiments using a real-time null-tracking algorithm, and the three coils operated by PCS with real-time feedback [26].

The present analysis is focused on comparing the standard divertor configuration and three stable SF configurations realized in the experiment. The SF configurations are characterized by the distance D between two divertor nulls, obtained from locating B_p null coordinates from magnetic equilibria reconstructions. The second B_p null coordinates can be also expressed in terms of normalized poloidal magnetic flux ψ_N so that the distance D is remapped to the radial midplane: the distance D_{mp} can be used to characterize the SF zone between nulls w.r.t. the SOL power width λ_q which is also typically expressed in units of outer midplane distance.

Shown in figure 2 are (1) the standard divertor with $D \geq 20$ cm (large); (2) the near-exact SF with $D \leq 0-5$ cm; (3) the SF-plus with $D \leq 10$ cm; (4) the asymmetric SF-minus with $D \leq 8-12$ cm. Other SF-minus configurations were also realized (not shown): the symmetric SF-minus, where both nulls are on the main separatrix, and another asymmetric SF-minus, where the secondary null is in the inner scrape-off layer (on the high-field side (HFS)) of the primary null. Because most of the inter-ELM power that escapes through the separatrix flows into the outer (LFS) divertor SOL, we focused here on the LFS SF-minus. However, we note that the HFS SF-minus configuration may be of interest for further studies of ELM heat flux mitigation, since higher peak heat fluxes from large ELMs are typically measured in the inner (HFS) divertor leg (strike point).

The SF configurations were produced for long periods, 2–3 s, i.e. many energy confinement times $\tau_E \leq 0.250$ s and comparable with the discharge flat-top duration of 3–4 s. Shown in figure 3 are typical time traces of two H-mode discharges with $P_{NBI} = 4.5-5$ MW, one with the standard divertor configuration, and another with the near-exact SF divertor configuration formed at 3.5 s and sustained for about 2.5 s. Generally, the SF configuration had weak, if any, effects on core plasma temperature, density or confinement [20, 23, 27, 28].

3. Results

The DIII-D experiments provided a comprehensive assessment of the SF divertor properties in a large tokamak with high divertor power loads and low-Z radiation. The experiments

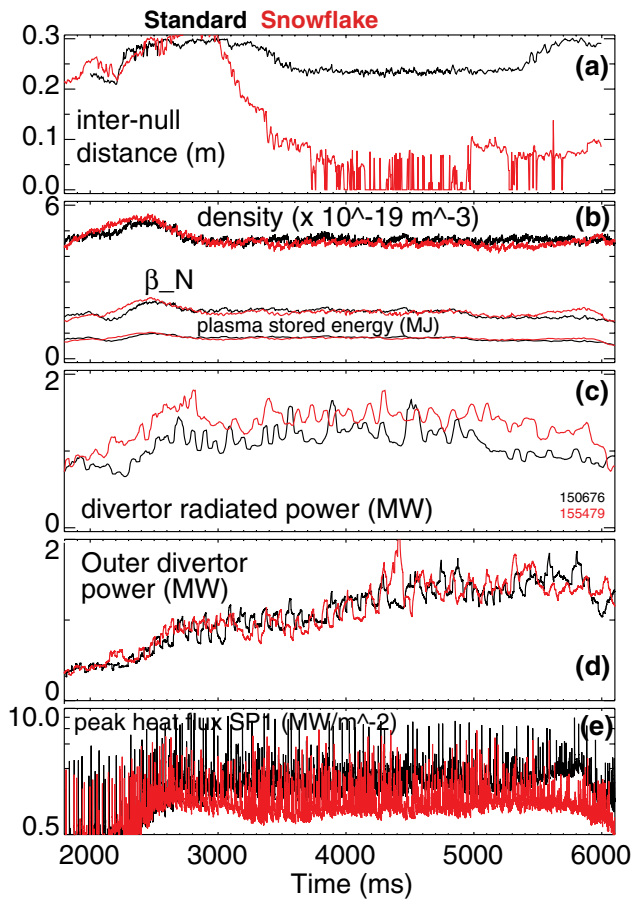


Figure 3. Time histories of two 1.2 MA H-mode discharges with the standard divertor ($P_{\text{NBI}} = 4.5$ MW, black time traces) and SF divertor ($P_{\text{NBI}} = 5$ MW, red traces). (a) Inter-null distance; (b) Core density, Plasma stored energy, and β_N ; (c) Lower divertor radiated power; (d) Power received by the lower divertor; (e) Peak divertor heat flux in SP1.

were aimed at clarifying the predicted SF effects (some of which were previously observed in the initial SF experiments on DIII-D and NSTX), including: divertor geometry effects and heat flux spreading, divertor heat and particle flux sharing between additional strike points, convective transport in the SF null region, and detachment onset and stability. The experiments also provided an assessment of SF effects on pedestal stability and ELMs presented elsewhere [27, 28].

3.1. Geometric properties of snowflake configurations

Divertor magnetic geometry modifications in the SF configuration are predicted to affect divertor heat and particle transport and power deposition in a favorable way because of increased conductive and radiative heat losses, increased diffusion, and a fast convective plasma redistribution [7, 11]. The geometric properties of the SF-plus and the SF-minus configurations are similar to those of the exact SF configuration when the inter-null distance D satisfies $D \leq a (\lambda_q/a)^{1/3}$, where a is the minor radius and λ_q is the SOL power width [11]. The criterion yields $D \sim 10$ cm for DIII-D discharge parameters ($a \simeq 0.60$ m, $\lambda_q \leq 2\text{--}3$ mm [29, 30]). The low B_p regions in the typical standard and SF divertor configurations are shown

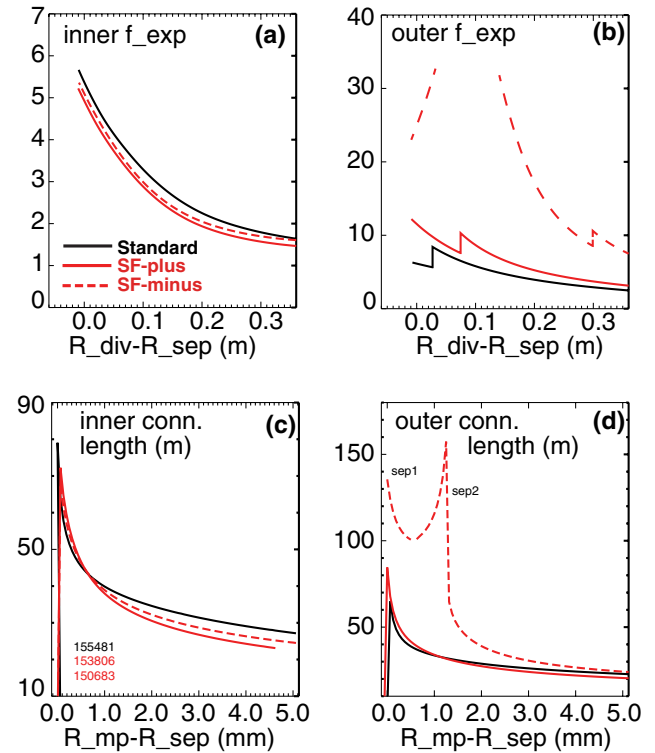


Figure 4. Geometric properties of the inner and outer SOL in the standard divertor (black lines) and SF divertors (solid red lines—SF-plus, dashed red lines—SF-minus). The magnetic flux expansion f_{exp} profile versus the distance from the primary separatrix strike point: (a) inner SOL, SP4; (b) Outer SOL. The midplane-to-target connection length l_{\parallel} profile versus the radial distance from the primary separatrix remapped to the midplane radius (see λ_q): (c) Inner SOL (inner midplane to inner target); (d) Outer SOL (outer midplane to outer target).

in figure 2. The low B_p zone was defined by the B_p contour at 10% of the mid plane separatrix B_p value. In the standard divertor, this zone was limited to the vicinity of the primary X-point. In the SF configurations, the zone was broader and often included the additional divertor legs and strike points. The latter is typical for compact divertor tokamaks, such as, e.g. DIII-D and NSTX.

The geometry properties realized in the SF divertor experiments in DIII-D included: (1) the formation of additional strike points (figure 2); (2) the increased connection length (a length of a field line connecting upstream midplane or X-point and the target (strike point))

$$l_{\parallel} = \int_{\text{SP}}^{\text{MP}} \frac{B_{\text{tot}}}{B_p} dl \quad (1)$$

(3) the increased specific divertor volume $V_{\text{div}} \sim l_{\parallel}$; (4) the increased poloidal flux expansion

$$f_{\text{exp}} = B_p^{\text{SP}} R_{\text{mp}} / (B_p^{\text{MP}} R_{\text{SP}}) \quad (2)$$

leading to the increased plasma-wetted area $A_{\text{wet}} = 2\pi R_{\text{SP}} f_{\text{exp}} \lambda_q / \sin(\theta)$, where $\sin(\theta)$ is the divertor target poloidal tilt angle. Significant geometry improvements in the SF divertor configurations are demonstrated in figure 4. Radial profiles of f_{exp} and l_{\parallel} are compared between the SF and the standard

divertor configurations for the inner SP4 and the outer SP1 regions. The inner divertor geometry was weakly affected in both the SF-minus and the SF-plus configurations. In the asymmetric SF-minus, the secondary null separated the outer SOL into two manifolds. In the manifold formed between the primary and secondary separatrices (that are defined by the nulls), both the f_{exp} and l_{\parallel} were increased significantly, by up to 70% between the separatrices and even higher closer to the separatrices. In the second, outermost SOL manifold, the geometry was modified to a lesser extent. In the SF-plus, the secondary B_p null (in the private flux region) mainly affected the geometry at the separatrix, within $\leq 10\%$ – 30% of the SOL width: modest increases in both the outer f_{exp} and the outer l_{\parallel} up to 30% were noted. In the near-exact SF (not shown), the flux expansion was similar to the SF plus, the connection length increase was stronger in the near-separatrix region.

3.2. Inter-ELM sharing of power and particle fluxes between snowflake divertor strike points

Power sharing over multiple strike points and cross-field (radial) transport modifications are viewed as attractive SF features. In this section, we discuss inter-ELM peak heat flux reduction and power and particle flow sharing observed in the SF divertor configurations (see standard divertor) in lower density H-mode discharges.

Heat and particle flux sharing effects were expected in the SF configurations produced in the experiment because of the following two arguments.

First, the divertor heat and particle deposition patterns in the SF divertor are defined in the first order by the relative magnitudes the SOL power width λ_q and the inter-null distance D [13] (here for comparison we use the inter-null distance mapped to the midplane D_{mp} (section 2). If $D_{mp} \ll \lambda_q$, the SOL ‘sees’ little difference between SF-plus and SF-minus configurations. The near-exact SF divertor configuration discussed below belongs to this case. If $D_{mp} \gg \lambda_q$, quasi-SF configurations close to the standard divertor are realized, with some SOL fraction affected by the weak B_p region. In the described DIII-D SF-minus and SF-plus experiments, both λ_q and D_{mp} were comparable: $\lambda_q \simeq 2$ – 3 mm, whereas $D_{mp} = 0$ – 5 mm. As predicted theoretically [13], in this situation the SF-minus and the SF-plus should produce differences in the SOL structure and sharing of the heat and particle fluxes between additional strike points, as compared to the two strike points of the standard divertor.

Second, according to the SF theoretical criterion, enhanced radial transport that leads to power sharing among multiple (four) strike points is activated when the high plasma convection zone radius $D^* \sim a(a\beta_{pm}/R)^{1/3}$ is comparable to the inter-null distance D [11]. This criterion yields $D^* \sim 10$ cm using the DIII-D parameters. In the experiment, distances $D = 0$ – 12 cm were typically realized, reaffirming the expectation that different transport properties could be measurable in the SF-plus and the SF-minus configurations. A comparison of $D_{mp} = 0$ – 3 mm and the SOL power width $\lambda_q \leq 2$ – 3 mm [29, 30] in the standard divertor suggests that the SOL power channel may be affected by the SF geometries.

Many inferred SF properties are based on the measured divertor heat flux profiles as follows. The heat flux analysis is based on infrared camera measurements of divertor surface temperature profiles as discussed in, e.g. [29, 30]. The inter-ELM profiles were conditionally averaged during the last 25% of the inter-ELM cycle (i.e. before each ELM) when the heat flux is fully relaxed. The conditional averaging used time periods of 30–100 ms duration, when the electron density n_e was matched within $\leq 10\%$ between the standard and the SF discharges. The density matching was important because the divertor radiated power loss is a strong function of upstream density in DIII-D. Edge and divertor radiation in these discharges were low, and similar within 10–15% between the SF and standard divertor, hence not a significant factor in the power balance. The effect of the increased A_{wet} on divertor heat footprint, while significant in DIII-D and NSTX, is not readily observed in tokamaks with target plates positioned further away from the SF null region, such as TCV [14] or some future designs [31, 32]. To account for the effect of A_{wet} (f_{exp}) in heat transport studies, the outer SOL parallel heat flux profiles are calculated and remapped from divertor major radius to midplane radial distance using EFIT magnetic equilibria reconstructions:

$$q_{\parallel} = q_{\text{div}} / \sin \alpha \quad (3)$$

where $\alpha = 0.5 - 2^\circ$ is the angle between the total magnetic field and the divertor plate. The outer SOL parallel heat flux profiles are shown in panels (c) in figures 5, 8, and 9 for the SF-minus, SF-plus and the near-exact SF configurations, respectively.

3.2.1. Snowflake-minus divertor. As discussed above, the second null in the SF-minus divertor configuration produces clear and significant magnetic geometry effect by splitting the outer SOL into two manifolds. This effect is clearly observed in divertor deposited heat flux profiles. Shown in figures 5(a) and (b) are the inner and outer divertor target heat flux profiles, respectively, measured in H-mode discharges with $P_{\text{NBI}} = 4$ MW and $n_e \sim (5 - 6) \times 10^{19} \text{ m}^{-3}$. While the inner SP4 heat fluxes were generally low, peak heat fluxes in the SF-minus divertor were higher by up to 15% over those of the standard inner divertor. Since the geometry of the inner divertor was unchanged, higher heat fluxes in the inner SP4 may be indicative of heat redistribution in the SF-minus over all strike points. Heat fluxes in the strike point SP3 (main separatrix) were only measurable in discharges with $P_{\text{NBI}} \geq 3.5$ MW. Heat fluxes in the secondary SP2 were practically unmeasurable. The flux expansion over the SP3 region was very high (30–40) resulting in small angles $\alpha \leq 1^\circ$. In addition, the connection length over the entire region was very high, also likely to result in additional dissipative losses. The secondary SOL (SP1) received a large fraction of heat, however, with much lower peak heat fluxes than in the standard divertor, to a large degree due to a wetted area (flux expansion) increase. Both the flux expansion and the connection length in the outer SP1 region were high, although to a lesser extent than in SP3.

Heat flux sharing between the SF-minus outer SOL manifolds is also clearly observed in the parallel heat flux profiles,

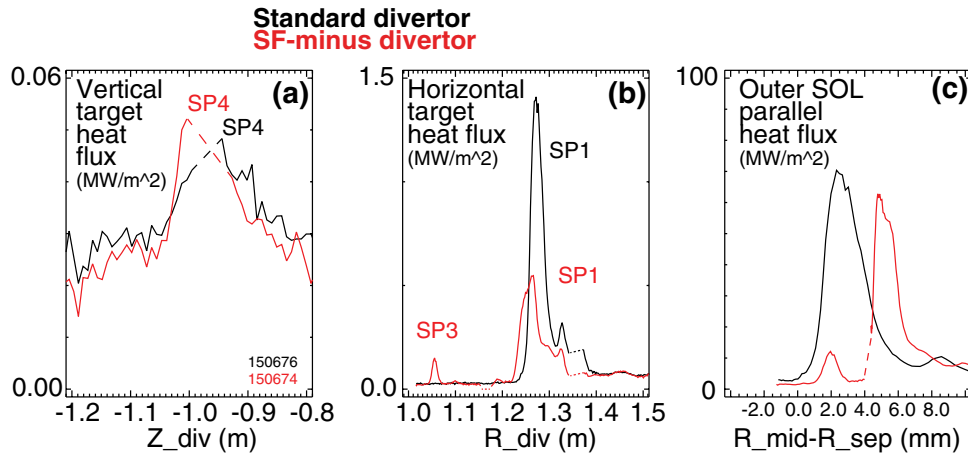


Figure 5. Inter-ELM heat flux profiles in the standard ($D \approx 20$ cm, black lines) and SF-minus ($D \leq 11$ cm, red lines) divertor configurations. (a) Vertical target (inner) divertor heat flux; (b) Horizontal and 45-degree tile outer target divertor heat flux; (c) Outer SOL parallel heat flux profiles versus radial distance from separatrix remapped to the outer midplane.

as shown in figure 5(c). Two peaks corresponding to the primary SP1 and secondary SP3 in the SF-minus divertor are evident. Heat flux profiles remained peaked and bell-shaped in both manifolds despite the fact that the upstream (midplane) heat flux is expected to be exponential-like. The amounts of heat partitioned between the main SOL (SP3) and the secondary SOL (SP1) are unknown since the SP3 heat deposition is likely to be affected by volumetric losses, with a possibility of full radiative detachment. The heat partition between SP1, SP2 and SP3 is an important feature of the SF-minus configuration and should be studied more systematically in future experiments, to complement the first studies presented below.

Inter-ELM power flow sharing between the primary and additional strike points in the SF-minus divertor is demonstrated in figure 6. The divertor power deposition (sharing) fractions in the SF-minus strike points were studied as a function of distance D between the nulls in a series of H-mode discharges with 4–5 MW NBI heating and $n_e \approx 4.8 - 5.0 \times 10^{-19} \text{ m}^{-3}$. The power deposition trends are unaffected by A_{wet} and reflect the SF power sharing. The divertor relative power fractions deposited in the spatial regions of the SP1 ($R = 1.23 - 1.37$ m), SP2 ($R = 1.13 - 1.23$ m), and SP3 ($R = 1.03 - 1.113$ m) on the outer divertor target in the SF-minus are compared to the standard divertor. The normalization is done to the total power deposited on the lower outer divertor target that includes the 45-degree section and the horizontal section. The distance D was varied from 20–30 cm (standard divertor) to 0–18 cm (SF-minus). Small power fractions below 10% were usually measured in the additional SF-minus strike point regions SP2 and SP3. A weak trend of increasing power in these strike points with decreasing D (approaching SF-minus) was evident. At $D \approx 20$ cm, the second null entered the SOL and split it into two manifolds, resulting in increase of power fractions directed to the SP2 and SP3. The data scatter around $D = 10$ –20 cm was due to the orientation of the two nulls: for the same D , the relative placement of the second null (D_{mp}) in the SOL could slightly vary, apparently affecting how the power was divided. Most power was deposited in the secondary SOL strike point SP1, however, it decreased with decreasing D by 20%, proportionally with power redistribution into additional

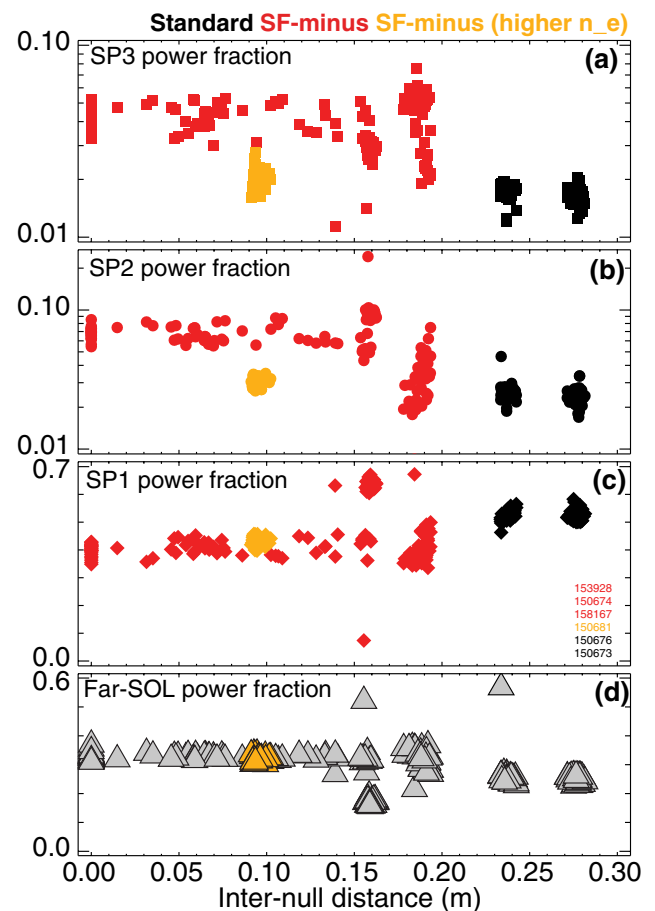


Figure 6. Relative fractions of outer divertor power deposited in the standard and SF-minus configurations as a function of inter-null distance D . Strike point regions are clarified in figures 2(d) and 5(b). (a) SP3 region ($R = 1.03 - 1.113$ m); (b) SP2 region ($R = 1.13 - 1.23$ m); (c) SP1 region ($R = 1.23 - 1.37$ m); (d) Far-SOL divertor shelf region ($R = 1.38 - 1.75$ m).

SF-minus strike points SP2 and SP3. A large power fraction, up to 35%, was deposited in the far-SOL region in all divertor configurations. This is somewhat unexpected, however, it is thought as mostly due to a large area (associated with the larger major radius) over which power density is integrated.

A weak increase of the integrated power in the far-SOL with decreasing inter-null distance (approaching SF-minus) is presently not understood. The flux expansion in the far-SOL was 15% higher in the SF-minus configuration, whereas the deposited heat fluxes were similar, suggesting that the parallel heat flux in the SF-minus could be slightly higher in the far-SOL.

Power fractions deposited in the additional strike points SP2 and SP3 in the SF-minus were found to be sensitive to upstream (divertor) density, as more power was radiated at higher densities. In figure 6, data for SF-minus at higher density ($n_e \simeq 6 \times 10^{-19} \text{ m}^{-3}$) indicated that at small D , additional strike point power was strongly reduced to the levels barely measurable by the IR camera (approaching the levels measured in the standard divertor private flux region). The main power was directed to the secondary manifold SP1 and the far-SOL at the same fractional levels (while the total deposited power was obviously reduced due to increased radiation at higher divertor density).

Significant heat redistribution and peak heat flux reduction take place in the SF-minus configuration due to SOL splitting and geometric mitigation factors in each SOL manifold, as highlighted in figure 7. Lower divertor heat flux profiles measured in the inner (SP4) and outer (SP3, SP2, and SP1) divertors in a series of H-mode discharges with varying input heating (NBI) power (proportional to P_{SOL}) $P_{\text{in}} = 1\text{--}10$ MW are shown. With increasing input power, the inner SP4 receives more heat in the SF-minus (see the standard divertor inner strike point). Also evident are (1) the absence of heat flux in SP3 at lower power, (2) a nearly-Gaussian shape of the SP3 heat flux profile at higher power. Both are suggestive of heat diffusion, a significant heat flux reduction due to increased plasma-wetted area (flux expansion), and possible SP3 detachment at lower power. The peak heat flux in SP1 was always significantly reduced as well. We note that the highest input power 10 MW ($P_{\text{NBI}} = 7$ MW and $P_{\text{ECH}} = 3$ MW) was used in the high-performance advanced tokamak H-mode, and the comparison was made between the standard double null (DN) configuration and the configuration with the upper standard divertor and the lower SF-minus (DN-SF), both with the ion ∇B drift toward the upper divertor [33]. The DN configuration was biased toward the lower single null with $dR_{\text{sep}} = -5$ mm (the distance between separatrices mapped to the midplane). The DN-SF configuration partitioned the outer SOL into three manifolds, separated by the SF-minus null ($D_{\text{mp}} = 2$ mm) and the upper DN null ($dR_{\text{sep}} = -5$ mm). A significant power fraction was directed to the lower outer divertor resulting in power deposition in SP1 and SP3 (figure 7(e)).

3.2.2. Snowflake-plus divertor. Inter-ELM heat flux redistribution and geometry effects in the SF-plus divertor appear to be more subtle than in the SF-minus, since the SOL geometry in the SP-plus configuration is not as drastically affected, in comparison with the standard divertor. Lower divertor heat flux profiles in the SF-plus divertor and the standard divertor are compared in figures 8(a) and (b). The profiles were measured in 4.5 MW NBI-heated low-density H-mode discharges. Peak heat fluxes were reduced by up to 50% in the outer SP1.

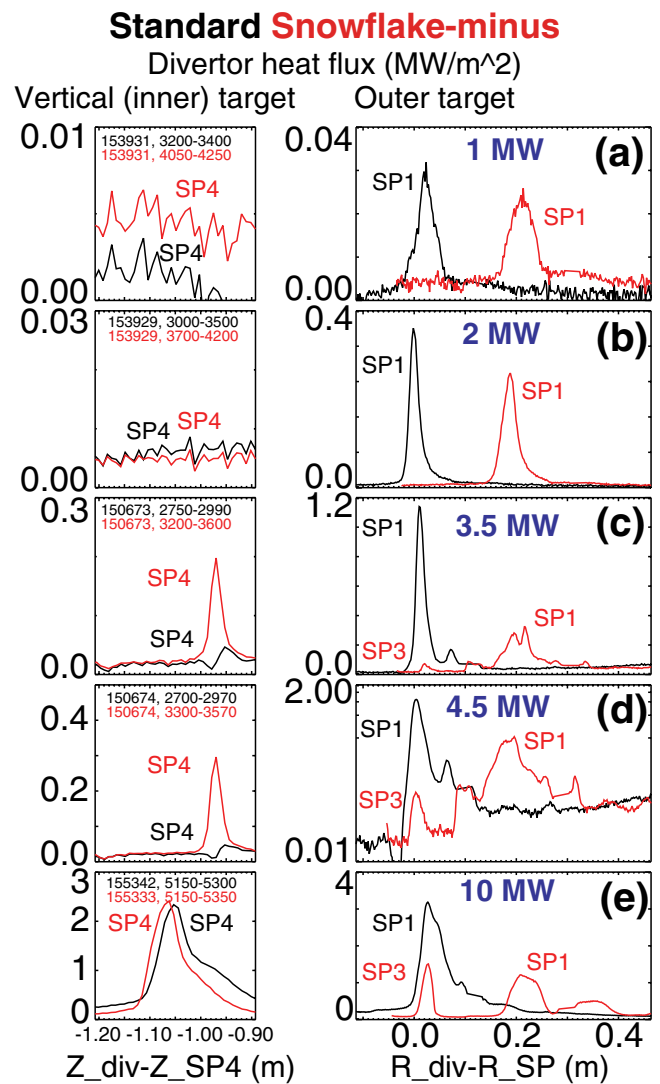


Figure 7. Divertor target profiles in the standard (black lines) and SF-minus (red lines) divertor configurations in H-mode discharges with different NBI heating powers. Inner (vertical) target profiles are shown in the left panels, outer (horizontal) target profiles are shown in the right panels. NBI input power ((a)–(d)) and NBI + ECH input power (d) are shown in the right panels.

The impact of increased plasma-wetted area (f_{exp}) on the heat deposition in the primary outer strike point SP1 was small, suggesting that other geometry and/or transport effects contributed to the heat flux reduction. This is supported by the outer SOL parallel heat flux profiles shown in figure 8(c). The q_{\parallel} profiles show peak reduction and profile broadening. The inner (vertical) target heat fluxes in SP4 were increased (albeit remaining at a very low level), again suggesting power redistribution in the SF-plus among the strike points. Heat deposition in the additional strike points SP2 and SP3 was rarely measurable.

3.2.3. Near-exact snowflake divertor. The analyses of particle and power flows in the near-exact SF divertor show clear redistribution trends. In the near-exact SF, the distance between the two nulls is maintained as low as possible. In this sense, the near-exact SF represents the merging of the SF-minus and SF-plus results at $D \rightarrow 0$. The time histories of the

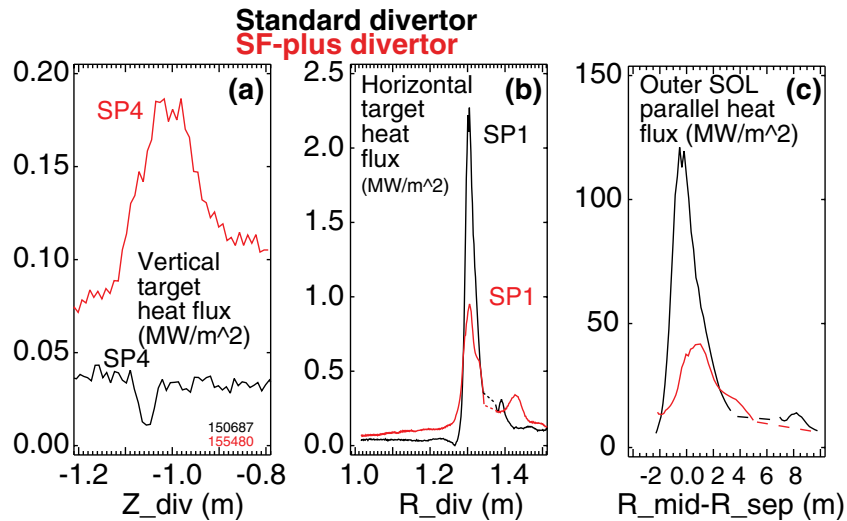


Figure 8. Inter-ELM heat flux profiles in the standard ($D \simeq 20$ cm, black lines) and SF-plus ($D \leq 10$ cm, red lines) divertor configurations. (a) Vertical target (inner) divertor heat flux; (b) Horizontal target divertor heat flux; (c) Outer SOL parallel heat flux profiles versus radial distance from separatrix remapped to the outer midplane.

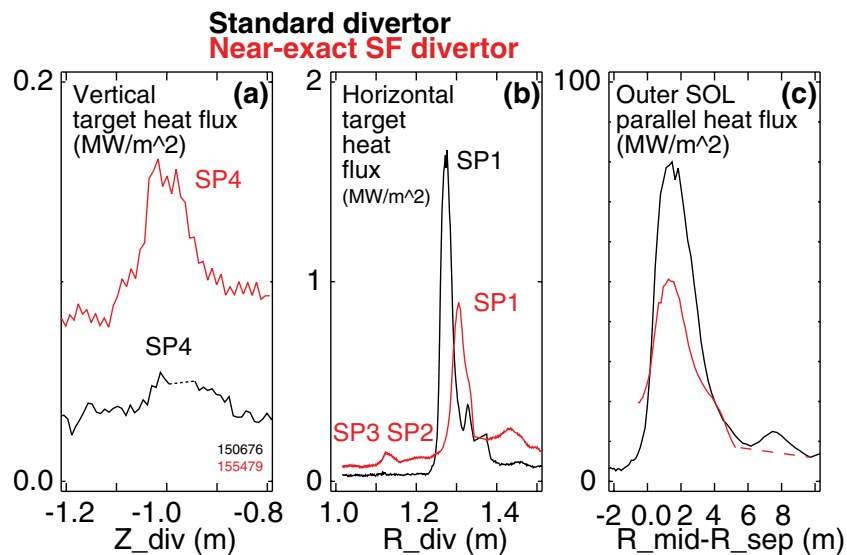


Figure 9. Inter-ELM heat flux profiles in the standard ($D \simeq 20$ cm, black lines) and near-exact SF ($D \leq 3$ cm, red lines) divertor configurations. (a) Vertical target (inner) divertor heat flux; (b) Horizontal target divertor heat flux; (c) Outer SOL parallel heat flux profiles versus radial distance from separatrix remapped to the outer midplane.

near-exact SF discharge are shown in figure 3: the distance D oscillated between 0 and 5–6 cm, while stable plasma characteristics (n_e , q_{peak}) were maintained. The divertor heat flux profiles shown in figures 9(a) and (b), as well as the outer SOL parallel heat flux profile (figure 9(c)), were qualitatively similar to the SF-plus profiles: in comparison with the standard divertor, peak reduction, profile broadening in the outer SP1, and peak increase in the inner SP4 were evident.

Particle flux sharing in the near-exact SF divertor between SP2, SP3, and SP4 strike points is demonstrated in figures 10(a)–(e). Divertor target Langmuir probe measurements were available for particle flux analysis in this discharge. Because of discrete Langmuir probe locations and few available probes, only qualitative characterization of particle flux using saturation current density J_{sat} measurements in the vicinity of the strike points was possible. Langmuir probe

J_{sat} time histories shown in figures 10(c)–(e) demonstrate that particle fluxes increased by 1–2 orders of magnitude in the innermost SP4, and in the additional strike points SP2 and SP3 after a transition from the standard divertor to the near-exact SF. In the inner SP4, however, the increase was also in part due to the drifting SP toward the probe LP6.

A comparison of power fractions deposited in the standard divertor and the near-exact SF divertor in strike point SP1, SP2, and SP3 regions (figures 10(f)–(h)) demonstrates significant power sharing. The power fraction trends for SP1, SP2 and SP3 with inter-null distance show that (1) power deposition was increased in the additional strike point regions (SP2, SP3), and (2) power deposition in the outermost strike point SP1 region was decreased by 30–40 % (about 0.3–0.4 MW in the near-exact SF versus 0.5–0.55 MW in the standard divertor). Divertor power deposition fractions were obtained

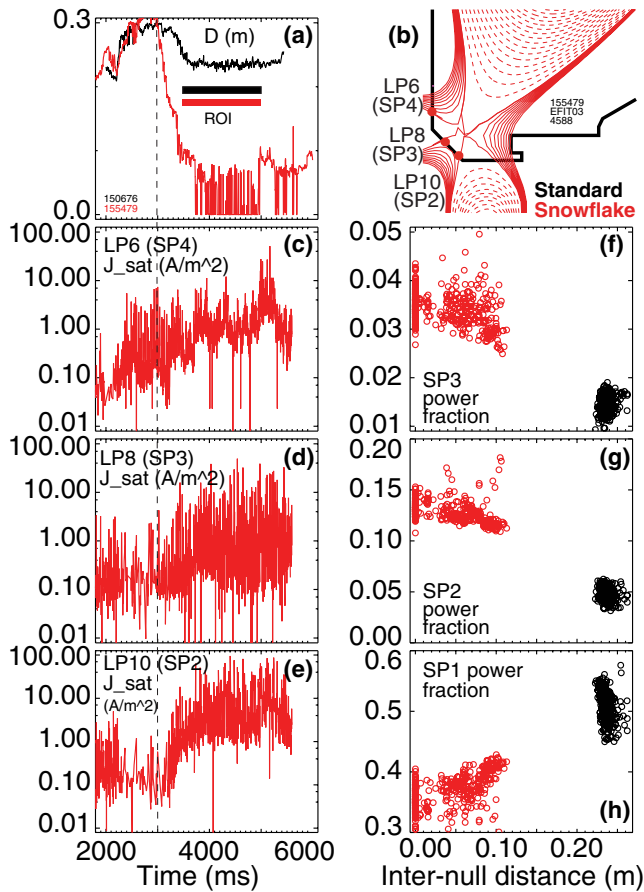


Figure 10. Details of particle and power flux sharing between SF strike points. (a) Time histories of inter-null distance D in the standard (black line) and near-exact SF (red line) divertor H-mode discharges; (b) The near-exact SF divertor magnetic equilibrium and locations of the Langmuir probes whose data shown in (c)–(e); (c) Saturation current density J_{sat} of probe LP6 in the vicinity of SP4; (d) Saturation current density J_{sat} of probe LP8 in the vicinity of SP3; (e) Saturation current density J_{sat} of probe LP10 in the vicinity of SP2. Lower divertor relative power fraction measured in the region of SP3 (f); SP2 (g); and SP1 (h) in the standard and near-exact SF divertor configurations.

for the strike points on the horizontal targets by integrating measured inter-ELM heat fluxes over the strike point regions (see figures 2(b) and 8 (b)) and normalizing the obtained SP power to the total power deposited over the entire divertor target area. It is noted that the SP2 and SP3 regions of the standard divertor are situated in the private flux region and receive very low heat fluxes from plasma radiation. The near-exact SF power fractions are consistent with those of SF-minus configuration at very low inter-null distances D presented in figure 6.

3.3. Plasma convection in the low- B_p region of the snowflake divertor

As demonstrated in the previous section, one of the key properties of the SF divertor configuration is the plasma spreading over additional divertor legs (strike points). A number of physical mechanisms that could be responsible for the spreading has been proposed theoretically [10, 11, 13, 34, 35], and simulated in a numerical model [36]. Classical electromagnetic

$E \times B$ drifts have been proposed to explain transport enhancements in SF separatrix branches [37]. Candidate instabilities (modes) that could cause the convection have been discussed [13, 34]: a toroidally symmetric convective cell with a plasma vortex (a ‘churning mode’) driven by the vertical plasma pressure gradient and toroidal field curvature [10, 11, 13, 35]; toroidal curvature-driven $n = 0$ flute-like modes [34, 38] or divertor ballooning modes [34, 39]; and MHD turbulence [13]. The onset of candidate modes depends critically on the plasma pressure across the separatrix, with the threshold values for mode onset expressed in terms of poloidal β_p :

$$\beta_p = P_k/P_m = 8\pi P_k/B_p^2 \gg 1$$

where P_k is the kinetic plasma pressure, and P_m is the poloidal magnetic plasma pressure. In the cases of the pressure-driven convection (the churning mode) and the ballooning modes, the onset depends not only on the pressure gradient, but also on the orientation of the snowflake configuration and the associated toroidal curvature. To maximize the drive terms, the churning mode needs a vertical pressure gradient, whereas the ballooning mode needs a radial pressure gradient. It is important to note that the candidate mode onset and the spatial extent may be significantly enhanced during ELMs when plasma pressure increases by orders of magnitude in the divertor at the arrival of the ion density transient from the pedestal with $T_i \sim T_i^{\text{ped}}$ [13, 34].

Experimental validation of the theoretically proposed convection mechanisms is not straightforward as the desirable mode parameters, e.g. its amplitude, frequency, or plasma vortex motion, are not readily measurable. In addition, in this work, we analyze SF properties between ELMs, where transport enhancements may be modest. In the following, we present measurements of time-averaged inter-ELM vertical pressure gradient profiles and β_p profiles and discuss their relation to the churning mode which was predicted to dominate over the other mechanisms [13]. The DIII-D measurements are a first step toward validating assumptions of the theoretical models.

The churning mode model elucidates a fast convective plasma redistribution in the poloidally localized and toroidally symmetric zone where poloidal β_p is high. Because of a broader region of weak B_p in the SF configurations, the high poloidal beta β_p region is also broader than that in the standard divertor X-point region. The pressure balance condition required for poloidal magnetic equilibrium no longer holds in the wider $\beta_p \gg 1$ zone: with a strong vertical pressure gradient and only toroidal field (but weak poloidal field) the equilibrium cannot be sustained. Plasma convective vortex motion onsets in order to compensate and recover the pressure balance condition [10, 11, 13, 35]. The mentioned theoretical references compared this convective cell instability to a neutral fluid in gravitational field instability where fluid convective motion is driven by interaction of a vertical gravitational force (the toroidal field curvature in the SF) and a horizontal thermal gradient (the vertical pressure gradient in the SF). The churning mode rotation was described either analytically using the Lagrangian description of the fluid element motion associated with the changes in the system’s thermal

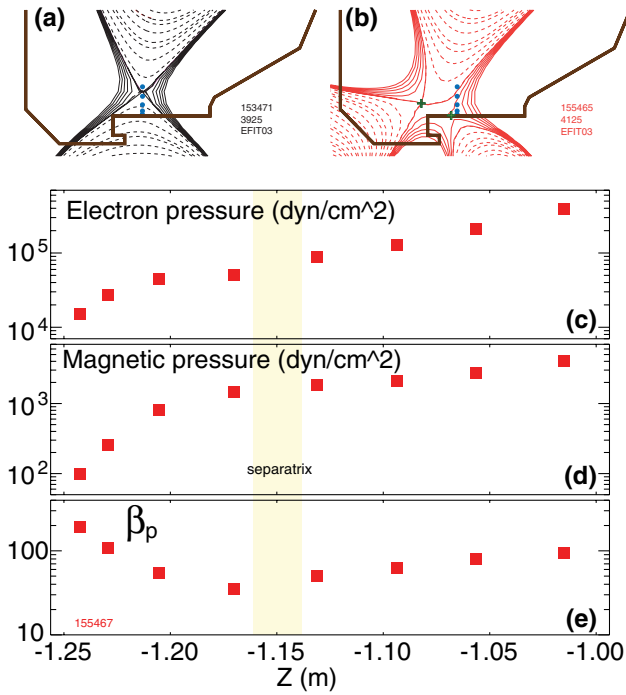


Figure 11. Magnetic equilibria used for DTS measurements: (a) standard divertor and (b) SF-minus divertor configurations. Vertical points show DTS measurements. SF-minus divertor profiles of (c) Electron pressure P_e ; (d) Magnetic pressure P_m , and (e) Poloidal beta β_p as a function of vertical distance (DTS measurement points).

and magnetic energies [10]; or by numerical integration of the reduced ideal MHD equations with dissipative terms [36]. Both model implementations show that in the SF divertor, the plasma pressure and magnetic flux are perturbed over a larger zone with a size that scales with poloidal β , as compared to the standard divertor.

Poloidal β_p profiles have been inferred for the standard and SF divertor configurations, as shown in figures 11 and 12, and confirmed the existence of the high β_p broad region in the SF configuration.

A unique DIII-D tokamak diagnostic, the divertor Thomson scattering (DTS) system [40–42], has been used to measure electron pressure $P_e = n_e T_e$. The kinetic pressure P_k was inferred under the assumption $P_k = P_e + P_i = 2P_e$ for the standard and SF null regions. Shown in figure 11 are the measurement geometry and the associated vertical profiles in the SF-minus divertor in the low density H-mode plasmas with $B_t = 2$ T, ion $B \times \nabla B$ toward the lower divertor, $I_p = 0.8$ MA and $P_{\text{NBI}} = 3$ MW. A special SF-minus scenario with $D_{mp} = 1\text{--}3$ mm was developed for these measurements, as the entire plasma had to be translated outward to intersect the vertical DTS measurement points, as shown in figure 11 (see figure 2). The scenario geometry is consistent with the theoretical assumptions of the churning mode formation discussed in [10, 13, 36]: the main separatrix orientation enables a strong vertical plasma pressure gradient. We note, however, that the measurements can be further improved by extending them outside of the SOL region, which was not possible with the present plasma control and DTS capabilities. In the standard divertor configuration, the P_e profiles were obtained by slow (1–2 s) non-perturbative translations of the X-point

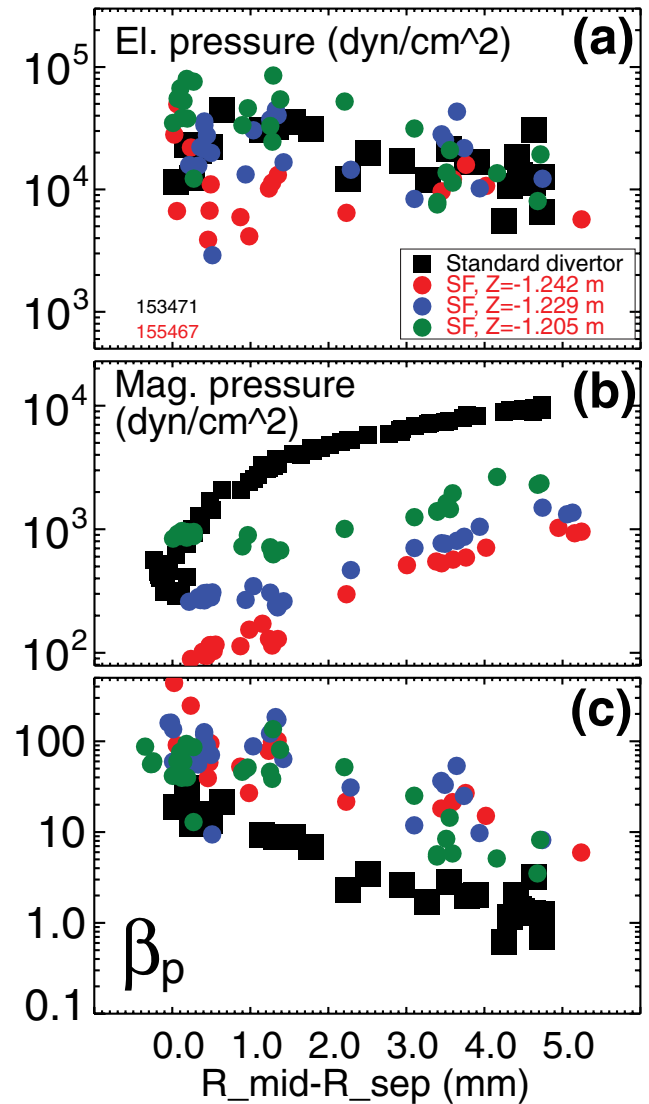


Figure 12. Divertor profiles as a function of distance from separatrix projected to midplane. (a) Electron pressure; (b) Magnetic pressure; (c) β_p . Note that the vertical profiles in the SF are remapped to radial midplane distance for comparison with λ_q . Standard divertor—black points, SF-minus divertor—colored points that correspond to the three points above the target ($Z_{\text{target}} = -1.250$ m) as indicated in figure 11: red— $Z = -1.2424$ m, blue— $Z = -1.2294$ m, green— $Z = -1.20540$ m.

horizontally across the DTS region using the plasma control system; in the SF configuration, the translation capability was limited to a few cm. The inter-ELM pressure P_e profiles were conditionally sampled between ELMs, with data points taken in several spatial locations above the divertor floor. The P_e and P_m profiles in the SF-minus configuration show a wide low B_p region and a strong vertical pressure gradient (going from the confined plasma inside the separatrix to the SOL plasma). The electron pressures measured in several spatial points with different ψ_N are similar throughout the SF null region, which may suggest plasma mixing throughout the region.

A comparison of the profiles measured in the divertor X-point(s) vicinity for the standard and SF-minus configurations is shown in figure 12. The scatter is caused by the DTS geometry that includes points on the same flux surface

ψ_N that have different vertical coordinate z . The profiles are projected to midplane radial distance from separatrix using ψ_N re-mapping. The standard divertor SOL power width at $I_p = 0.8$ MA is ≈ 3 mm [30]. The measurements suggest several interesting points. First, the kinetic pressure P_k ($2 \times P_e$) profiles in the standard and the SF-minus divertor were comparable, while P_m profiles significantly decrease toward the vicinity of the X-point(s). As a result, the divertor β_p profile is peaked in the X-point vicinity. The P_m is much lower in the SF, leading to significantly higher divertor β_p . Second, the region of high $\beta_p \geq 1$ is much broader in the SF configuration, essentially extending over the entire SOL width. For comparison, the measured upstream SOL $\beta_{pm} \leq 0.01$. Based on the theoretical estimates [10, 11] with DIII-D tokamak parameters, we obtain for the size of the convective zone D^* [10, 13]: $D^* = 0.81a(\beta_{pm}a/R)^{1/3} \sim 7$ cm for the SF, and $D^* = 0.44\beta_{pm}a^2/R \sim 0.1$ cm for the standard divertor. Using the estimated D^* , one can infer the churn period in the SF as $\tau = 1.3\sqrt{RD^*}/(\sqrt{2T/m_i}) \sim 10^{-5}$ s. This is typically much shorter than the Bohm diffusion time, or the parallel SOL transit time [10]. During ELMs, the null-region plasma pressure significantly increases due to the ELM ion density convective pulse, and D^* is further increased. The DTS measurements in DIII-D between ELMs confirm existence of the high β_p broad region in the SF configuration. While it is not presently possible to directly measure the hypothetical mode frequency or amplitude, present divertor β_p measurements can aid further modeling of β -dependent convective transport.

3.4. SOL power width in the snowflake divertor

Understanding parallel heat flux spreading in SF divertor configurations is key to future plasma device applications. Inter-ELM particle and power deposition on the divertor target in the divertor SOL is determined by the balance between parallel and cross-field SOL transport. Both of these processes are strongly linked to normalized SOL collisionality ν^* (or ν_{ee}/I_{\parallel} , where ν_{ee} is the electron collisionality) via parallel temperature gradient and radial pressure gradient, respectively, and further connected to turbulence. In the standard divertor SOL, particle and power widths may be related to transport and geometry (connection length) in a simplified way as follows. For plasma particles, the SOL width is estimated as $\lambda = \sqrt{D_{\perp}\tau_{\text{SOL}}} = \sqrt{D_{\perp}I_{\parallel}/v}$, where τ_{SOL} is the characteristic particle SOL time in a collisionless (low ν^*) regime, D_{\perp} is an effective diffusion coefficient, and v is the particle thermal speed. For energy (heat) transport, $\lambda_q \sim \sqrt{\chi_{\perp}\tau_{\parallel}^E}$, where $\tau_{\parallel}^E \sim (\pi qR)^2/(2\chi_{\parallel})$ is the energy loss time due to conduction and convection, and χ_{\perp} is determined by turbulence, classical drifts, and MHD. In the SF divertor, however, depending on parallel and cross-field transport mechanisms (diffusive versus convective), a longer connection length obtained thanks to lower B_p (see standard divertor), may not necessarily lead to an increased SOL width [43].

Recently, significant tokamak research efforts have been dedicated to elucidating λ_q and its dependencies on physics

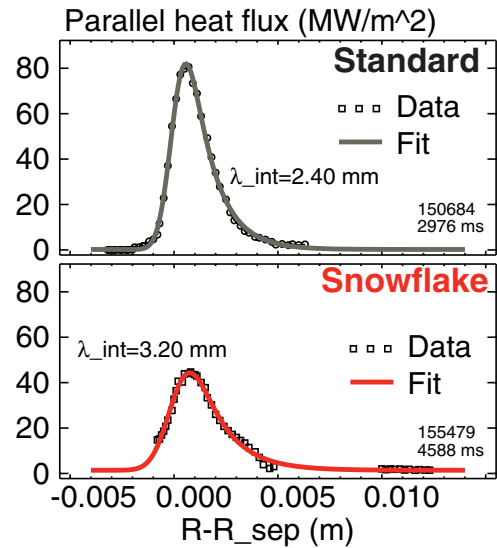


Figure 13. Inter-ELM parallel outer divertor (SP1) heat flux profiles in the standard and near-exact SF divertor configurations.

and engineering parameters [30, 44–46]. These arguments set qualitative expectations for the SF divertor. The cross-field transport in the SF divertor legs may be determined by local physics and weakly correlated with the upstream properties. This is because the SF configuration can lead to de-correlation (disconnection) of turbulence between upstream and downstream SOL due to flux tube shearing by very low B_p and the convective plasma redistribution in the null(s) region (e.g. the churning mode). The increased X-point connection length over a fraction of the SOL may result in a broader SOL. The classical $E \times B$ drift may also be enhanced in the low B_p region due to higher parallel temperature and density gradients that drive additional poloidal E terms. These effects may lead to the broadening of the SOL power channel (increasing the width λ_q). Attributing the broadening to a specific mechanism (or mechanisms) quantitatively appears to be beyond the present experimental capabilities.

In SF configurations, analyses of inter-ELM parallel heat flux profiles showed the outermost SP1 heat flux profile broadening by up to 50%. An example of the data and fitting is shown in figure 13, where parallel heat flux profiles in the standard and near-exact SF configurations of two low n_e H-mode discharges are compared. The integrated λ_q was broader and the peak q_{\parallel} was lower in the SF divertor configuration. Recent parallel heat flux width studies in DIII-D indicate that λ_q scales with inverse I_p (B_p), and is consistent with B_p -dependent cross-field SOL transport models [29, 30]. As in [30], the measured $q(R_{\text{div}})$ was mapped to q_{\parallel} as a function of the radial midplane distance from separatrix. The profile was fitted with the Eich function [44], a sum of the Gaussian function and the exponential function, the former characterizing symmetric radial heat spreading into the SOL and private flux region via the spreading parameter S , and the latter characteristic of the SOL transport via the SOL power width λ_{SOL} : $\lambda_{\text{Eich-int}} \simeq \lambda_{\text{SOL}} + 1.64 S$.

The parallel heat flux width trend as a function of inter-null distance D was studied in a number of near-exact SF, SF-plus and SF-minus configurations. Shown in figure 14

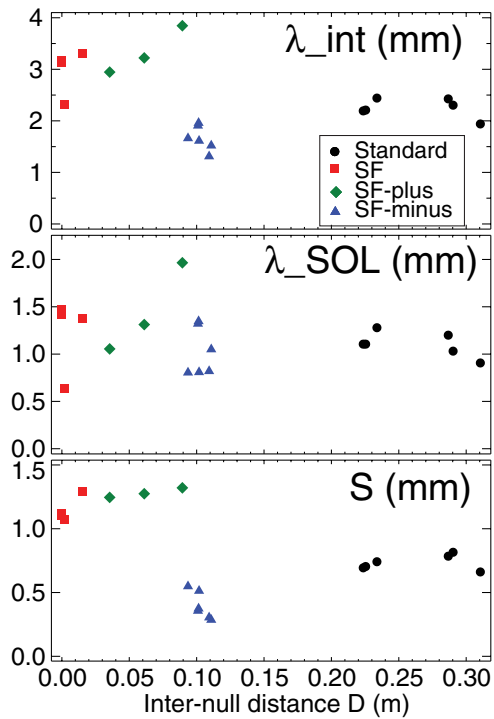


Figure 14. Outer midplane power widths (SP1) as a function of inter-null distance D for the standard, SF-minus, SF-plus, and near-exact SF in 1.2 MA H-mode discharges. (a) Integral SOL width λ_{int} ; (b) SOL width λ_{SOL} ; (c) Spreading parameter S .

are the integral SOL width λ_{int} , and the two λ_{int} components, λ_{SOL} and S for the outermost SP1 in the standard and SF divertor configurations. The data points were from conditionally-averaged (between ELM) heat flux profiles measured in $P_{\text{NBI}} = 4.0\text{--}5.0$ MW 1.2 MA H-mode discharges with lower-end n_e densities and low divertor P_{rad} both matched within 15% between the discharges. Several interesting observations are noted.

Larger q_{\parallel} widths were observed in the near-exact SF and the SF-plus. In the near-exact SF and SF-plus divertors, the SOL widths λ_{SOL} were greater by up to 30%, whereas the S parameter was greater by up to 50%, as compared to the standard divertor. The λ_{int} increase in the SF was significant, by up to 50%. However, present data does not allow clear separation of the effects involved in the parallel heat flux profile changes. The obvious (local to the divertor) candidate mechanisms for the peak parallel heat flux reduction are the dissipative losses from the increased connection length l_{\parallel} , the increased diffusive spreading, and the power redistribution between the strike points. The λ_{int} increase appears to be mostly due to S , which may be from the increased dissipative losses and diffusive spreading. The increased λ_{SOL} in the SF divertor is an encouraging result since it may imply increased radial transport ($\lambda_q^2 \sim \chi_{\perp} \tau_E^{\text{SOL}}$).

The SF-minus data is more difficult to interpret, however, it is also shown in figure 14 for comparison. In the SF-minus, the secondary null separates the SOL into two manifolds connected to the primary SP3 and secondary SP1. As discussed in section 3.2, heat flow in the SP3 was significantly affected by the SF geometry (e.g. l_{\parallel} increased by up to 70%, also

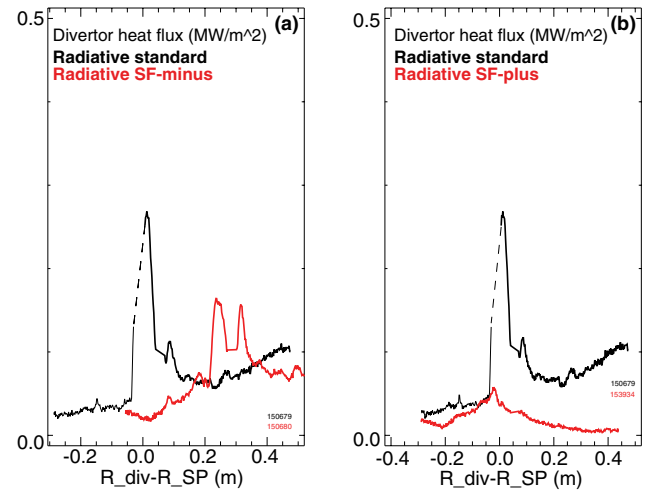


Figure 15. Horizontal divertor target profiles in the standard radiative (black lines) and radiative SF (red lines) H-mode discharges.

increased A_{wet}): q_{peak} was barely detectable at $P_{\text{SOL}} \leq 3$ MW. Here, the SP3 widths were not plotted due to large uncertainties. However, the SP3 profiles at higher powers were measurable and appeared to be Gaussian-shaped (e.g. figures 6 and 7). The second (secondary) SOL manifold with SP1 is also affected by the SF-minus geometry: the SP1 separatrix borders the SP3 region, the secondary null, and its own private flux region. In the SP1, λ_{SOL} was similar to the standard divertor and S was smaller.

3.5. Radiative snowflake divertor

An important aspect of the SF divertor studied in DIII-D was the radiative SF divertor. The DIII-D experiments revealed stronger inter-ELM divertor peak heat flux reduction in the radiative SF divertor in comparison with the standard radiative divertor. Radiative divertor conditions in DIII-D are achieved in the standard divertor with carbon and deuterium radiation using D_2 seeding that increases upstream (and core) density [47, 48]. Preliminary results from the DIII-D radiative SF experiments have been previously discussed in [20, 23, 27, 33].

Both the radiative SF-plus and SF-minus divertors were compatible with good H-mode confinement albeit with confinement degradation similar to the standard radiative divertor. While the confinement degradation was not associated with the SF formation at lower-to-medium densities, additional D_2 seeding at rates 50–80 $\text{thinsp;Torr thinsp;l s}^{-1}$ (to raise the density for radiative divertor onset) resulted in 10%–20% reduction in, e.g. H98(y,2) and H89L factors and plasma stored energy W_{MHD} in the standard divertor, and up to 30% in H-mode discharges with the radiative (higher-density) SF-plus or SF-minus. The degradation was associated with the reduction of pedestal T_e^{ped} and the corresponding pedestal energy reduction [23]. Generally, reduced pedestal stability at higher collisionality is an expected effect of the radiative divertor on the confined plasma [49]. Further H-mode scenario development is necessary to optimize compatibility of the core plasma

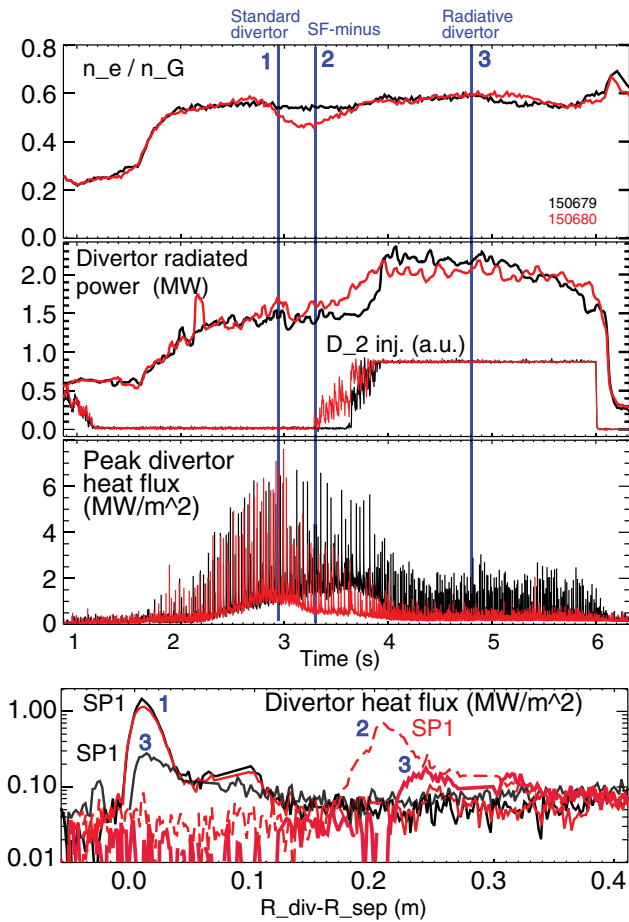


Figure 16. Time histories of radiative divertor H-mode discharges: black lines—standard divertor, red lines—SF-minus divertor configurations. (a) Core density normalized to Greenwald density n_G ; (b) Divertor radiated power and gas flow rate; (c) Peak divertor heat flux; (d) Horizontal divertor target heat flux profiles at times 1, 2, 3 indicated by blue vertical lines in (a)–(c).

with the radiative SF, as is typically done with the standard radiative divertor [50].

The reduction of inter-ELM divertor heat fluxes was stronger in the SF-plus and SF-minus configurations. Shown in figure 15 are outer divertor heat flux profiles in D_2 -seeded radiative SF and standard radiative divertor $P_{\text{NBI}} = 4$ MW H-modes at $\bar{n}_e = 6.3 - 6.8 \times 10^{-19} \text{ m}^{-3}$. In the standard divertor, the partial detachment led to a significant (up to a factor of 10) peak heat flux reduction (see figure 5 and 7–9). In the radiative SF-minus and SF-plus, a nearly complete power detachment was observed at 4 MW NBI power, as heat flux in SP1 was barely detectable.

Time histories of the 4 MW NBI-heated H-mode discharges with the standard radiative divertor and the SF-minus radiative divertor are shown in figure 16. In both cases, the core density was matched, leading to $P_{\text{SOL}} \sim 3.0 - 3.5$ MW and similar divertor radiated power 2 MW ($P_{\text{div}}^{\text{rad}} \simeq 0.55 - 0.65 P_{\text{SOL}}$) at higher density. Referring to the time histories in figure 16 and the divertor heat flux profiles in figure 16(d), at time ‘1’, when both discharges were in the standard divertor phase, divertor heat flux profiles were similar (SP1). By time ‘2’, the SF-minus divertor configuration was established, and the peak heat flux was reduced in SP1 (mostly due to the poloidal

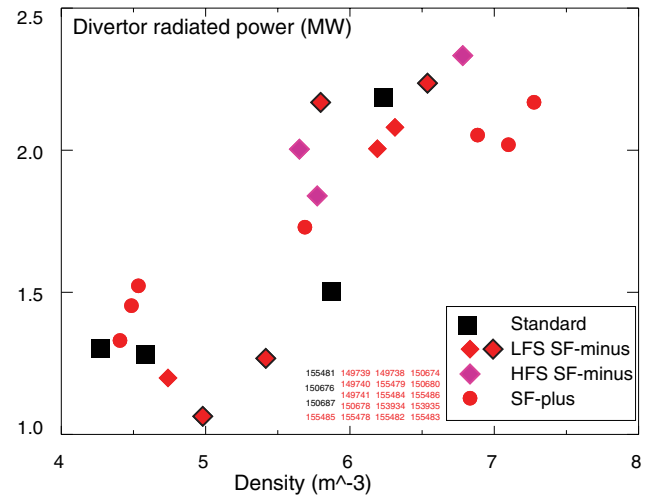


Figure 17. Divertor radiated power as a function of average core density for 1.2 MA, 4 MW NBI-heated H-mode discharges with standard divertor (black points) and SF (red points) divertor configurations.

flux expansion, as discussed earlier in section 3. By the time ‘3’, the gas flow was established and the upstream density increased, and the radiative conditions were realized for both configurations. The peak divertor heat flux (SP1) was lower in the radiative SF-minus in comparison with the standard radiative divertor. The flux expansion factor could still account for most of the difference between the radiative SF-minus and the standard divertor. In comparison with this radiative SF-minus observation, in the SF-plus configuration, the SP flux expansion was not as high, and could not fully account for the difference. Experiments at high P_{SOL} are needed to study differences in detachment characteristics between the SF and the standard divertor. One notable observation discussed in detail elsewhere [28] was the significant ELM peak heat flux reduction in the radiative SF minus (figure 16).

The onset of radiative SF conditions (e.g. increase in divertor impurity radiation and recombination, heat flux reduction) were obtained at core n_e similar within 10–20% to the standard radiative divertor. Shown in figure 17 is a trend of divertor P_{rad} versus average core density. In both standard and SF configurations, divertor temperature is reduced and the divertor radiation increases by 50% in a step-like manner at the the detachment onset. Present data includes crude n_e steps and does not allow to compare the detachment n_e onset conditions to better than 10–20% in terms of n_e .

While total divertor radiation levels were similar in the standard and SF radiative divertor experiments, spatial distributions differed. Divertor radiated power from carbon and deuterium species was distributed more broadly and uniformly in the radiative SF configurations. Spreading the radiation could be an additional benefit as it reduces radiated power density gradients and the peak radiative heating of divertor targets. Shown in figure 18 are the C III emissivity and total radiated power distributions in the radiative standard and SF divertor discharges discussed above ($P_{\text{rad}}^{\text{div}} \simeq 2$ MW). The C III emissivity distributions were obtained from tangential divertor cameras using a numerical inversion to convert line-integrated brightnesses to emissivities [48]. The total radiated power

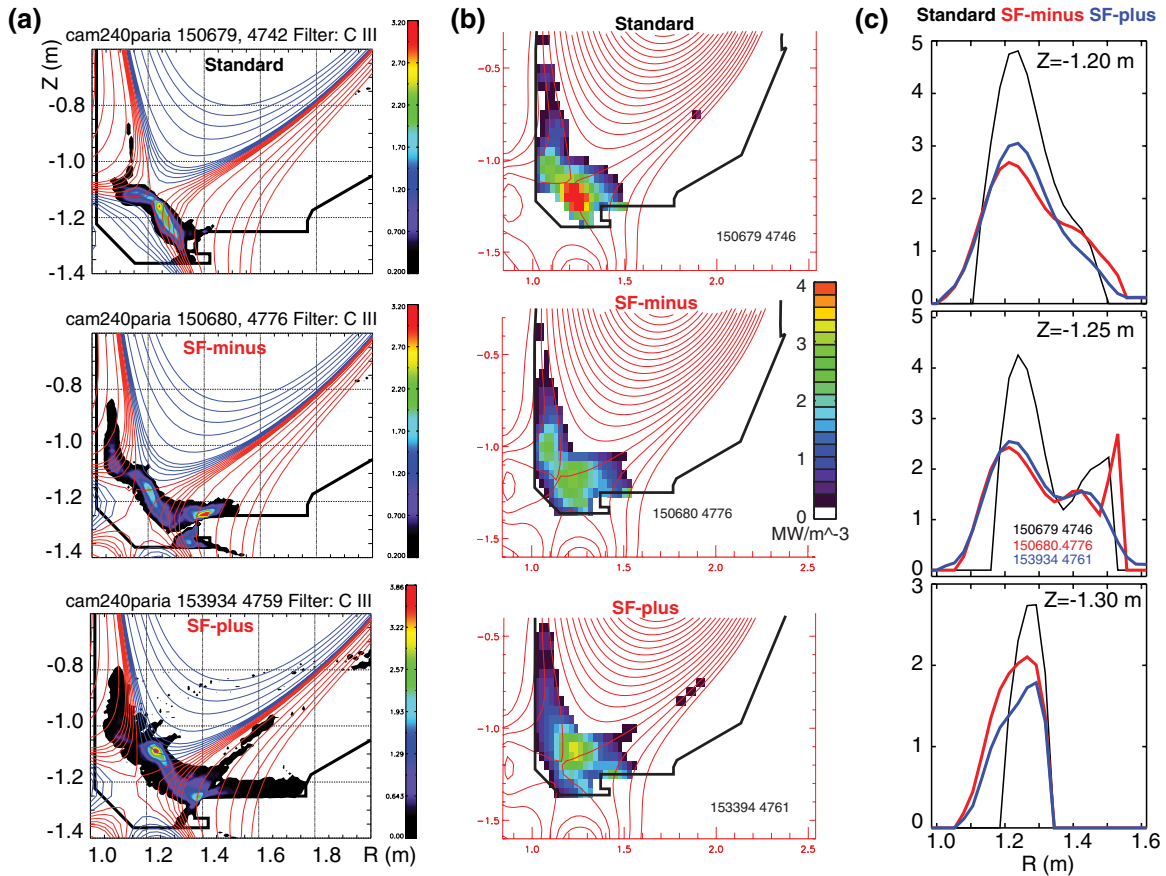


Figure 18. Carbon ion C III emissivity and radiated power density distributions in radiative standard, SF-minus, and SF-plus divertor configurations. (a) Divertor camera C III emissivities (note similar emissivity scales); (b) Radiated power density (same scale) obtained from tomographic bolometer inversions; (c) Radial profiles of radiated power density from (b) taken at $Z = -1.20$ m (X-point region), $Z = -1.25$ m (mid-leg region), and $Z = -1.30$ m (outer strike point region).

distributions were obtained from tomographic reconstructions of multi-channel bolometry data [51]. Both the divertor camera and the bolometer measurements were performed on a slow time scale (~ 30 ms), hence the the C III emissivity and the total plasma emissivity were average measurements that included ELMs. In the standard divertor, radiation initially peaked in the inner and outer divertor legs, and at the partial detachment onset, the radiative front moved to the X-point (e.g. [48]). In figure 18, both C III and total $P_{\text{rad}}^{\text{div}}$ are localized to the divertor leg and peak at the X-point. In contrast, in the SF-minus, radiation also initially peaked in the divertor legs, and with the SF-minus formation, it was broadly distributed throughout the divertor volume, with occasional peaking at the null-points. In the SF-plus, the radiation front was formed in the divertor legs and moved toward the null-point region where it stabilized. The extended connection length region enabled a broader radiation zone. Shown in figure 18(c) are $P_{\text{rad}}^{\text{div}}$ horizontal profiles at several elevations above the horizontal divertor target. The profiles demonstrate broader distribution and lower peaking of $P_{\text{rad}}^{\text{div}}$ in the radiative SF configurations. The data also shows that despite the increased I_{\parallel} by 50%–75%, the radiative SF configurations were not more likely than the standard divertor to form X-point radiative instabilities that could degrade the confinement.

4. Discussion and conclusions

Snowflake divertor configurations have been realized in DIII-D for several seconds in H-mode discharges with heating power $P_{\text{NBI}} \leq 4\text{--}5$ MW and a range of plasma currents $I_p = 0.8\text{--}1.2$ MA. For the first time, inter ELM transport and radiative SF divertor properties have been studied. Significant impact of geometric properties, such as increased f_{exp} , J_{\parallel} , V_{div} , on SOL plasma parameters has been shown. In the SF-minus configuration, heat deposition is affected by the geometry, and peak divertor heat fluxes are significantly reduced. In the SF-plus and near-exact SF configurations, divertor peak heat flux reduction and outer strike point heat flux profile broadening are observed. Inter-ELM sharing of power and particle fluxes between the main and the two additional snowflake divertor strike points has been demonstrated. The additional strike points typically receive up to 10–20% of the total outer divertor deposited power. Measurements of the vertical electron pressure profiles and the poloidal beta β_p support the theoretically proposed churning mode driven by the toroidal curvature and vertical pressure gradient and causing convective plasma redistribution in the weak B_p region. The radiative SF divertor leads to a nearly complete power detachment with 4–4.5 MW NBI heating and broader divertor radiated power

distribution. However, no significant difference in the detachment n_e threshold between the standard divertor and the SF divertor was found.

The reported snowflake divertor experiments can be related to experimental studies conducted in TCV and NSTX, and numerical modeling results. In particular, in TCV H-modes, up to 20 % of the ELM energy was found to be redistributed to the additional SPs while the primary SP peak heat flux was reduced by a factor of 2–3 [16]. The trends of power distribution between additional strike points in the SF-minus divertor configuration were studied numerically using the EMC3-EIRENE code (however, without drifts and impurities) [52]. The relative power fractions were found to depend on the position of the secondary separatrix in flux space rather than the inter-null distance D . In most DIII-D SF-minus configurations, the orientation of the nulls (angle) was similar, while both D and D_{mp} change proportionally. Hence, the SP power fractions showed similar trends as functions of D and D_{mp} . Radiative snowflake divertor and susceptibility to radiation limits were studied in NSTX with D_2 and CD_4 seeding [17, 18, 20], and TCV with D_2 and Ne [53], and did not show any significant difference in radiative instability likelihood between the snowflake divertor and standard divertor.

The DIII-D findings provide a basis for further transport studies of the SF divertor. A variety of the obtained SF configurations resulted in a large spectrum of geometries that need to be analyzed in detail w.r.t. the theoretically proposed plasma convection paradigm. A number of modes, including the churning mode, have threshold onset values that are functions of field (B_p), geometry ($l_{||}$, pressure gradient ∇p , toroidal field curvature ($\sim \epsilon/R$), and more generally, poloidal flux surface orientation), and plasma parameters (p, T_i). Both modeling and improved measurements are needed to understand the transport mechanisms better. As fluctuations of the above quantities are also important, direct measurements of turbulence characteristics in the SF region and their comparison to standard divertor and midplane turbulence are desirable.

The reported DIII-D measurements suggest increased inter-ELM SOL transport in the SF configurations. However, based on the results it is not possible to isolate a particular mechanism, such as, e.g. the convective instability or the increased $l_{||}$. Given that weak between-ELM plasma redistribution between additional strike points was observed, on the order of 10%, additional experiments are needed to clarify the effect. The measurements were severely limited by plasma control capabilities and could be further improved. One could envision an experiment in which the inter-null distance D would be varied on a slow (transport) time scale over 1–3 s, and a corresponding analysis of λ_q would follow. The experiment was attempted on DIII-D, however, inconclusive results were obtained due to poorly controlled SF configurations. In particular, a relative orientation of the nulls at medium-to-lower D appeared to be difficult to control. Ongoing work in SF real-time control is attempting to address these shortcomings [26].

Another possible experiment that could test SF perpendicular heat transport models and trends is a variation of plasma current, similar to the experiments studying λ_q 's as a function

of plasma current in the standard divertor [30]. A limited SF divertor data set was obtained in DIII-D in discharges with $I_p = 0.8, 0.9, 1.2$ and 1.5 MA. Quantitative conclusions on λ_q could not be reached due to the quality of SF configurations and the need to improve SF control in discharges with various plasma currents.

The radiative SF results in DIII-D are encouraging, however, some questions remain. While interesting observations have been made, e.g. the broader radiation distribution and peaking around additional nulls, it is puzzling that the SF geometric features do not always translate to larger differences in total radiated power. Additional experiments could improve divertor radiation distribution results and conclusions, possibly with improved plasma control capabilities, or seeding different impurities to probe different temperatures along the parallel T_e profile. However, the explanation could also be due to a physical mechanism limiting radiated power in the SF divertor.

In summary, the emerging understanding of inter-ELM divertor heat transport and radiation distribution in the SF divertor from recent DIII-D experiments provides support to the snowflake divertor concept as a promising solution for divertor heat flux mitigation in future magnetic fusion devices.

Acknowledgments

This work was performed under the auspices of the U.S. Department of Energy under Contracts DE-AC52-07NA27344, DE-AC02-09CH11466 and DE-FC02-04ER54698. This material is based upon work supported by the U.S. Department of Energy, Office of Science, Office of Fusion Energy Sciences. DIII-D data shown in this paper can be obtained in digital format by following the links at https://fusion.gat.com/global/D3D_DMP.

We thank the entire DIII-D Team for technical, engineering and computer support, as well as for plasma and diagnostic operations. Dr J.A. Boedo (UCSD) is gratefully acknowledged for data and analysis discussions.

ORCID iDs

V.A. Soukhanovskii  <https://orcid.org/0000-0001-5519-0145>

A.W. Leonard  <https://orcid.org/0000-0001-9356-1074>

References

- [1] ITER Physics Expert Group on Divertor, ITER Physics Expert Group on Divertor Modelling and Database and ITER Physics Basis Editors 1999 *Nucl. Fusion* **39** 2391
- [2] Loarte A. *et al* 2007 *Nucl. Fusion* **47** S203
- [3] Peng Y.-K. *et al* 2005 *Plasma Phys. Control. Fusion* **47** 263
- [4] Chan V. *et al* 2011 *Nucl. Fusion* **51** 083019
- [5] Zohm H. 2013 *Fus. Eng. Des.* **88** 428
- [6] Soukhanovskii V.A. 2017 *Plasma Phys. Control. Fusion* **59** 064005
- [7] Ryutov D. 2007 *Phys. Plasmas* **14** 064502

- [8] Ryutov D., Cohen R., Rognlien T. and Umansky M. 2008 *Phys. Plasmas* **15** 092501
- [9] Ryutov D., Makowski M. and Umansky M. 2010 *Plasma Phys. Control. Fusion* **52** 105001
- [10] Ryutov D., Cohen R., Farmer W., Rognlien T. and Umansky M. 2014 *Phys. Scr.* **89** 088002
- [11] Ryutov D., Cohen R., Rognlien T. and Umansky M. 2012 *Plasma Phys. Control. Fusion* **54** 124050
- [12] Ryutov D. and Umansky M. 2010 *Phys. Plasmas* **17** 014501
- [13] Ryutov D.D. and Soukhanovskii V.A. 2015 *Phys. Plasmas* **22** 110901
- [14] Piras F. et al 2010 *Phys. Rev. Lett.* **105** 155003
- [15] Reimerdes H. et al 2013 *Plasma Phys. Control. Fusion* **55** 124027
- [16] Vijvers W. et al 2014 *Nucl. Fusion* **54** 023009
- [17] Soukhanovskii V. et al 2011 *Nucl. Fusion* **51** 012001
- [18] Soukhanovskii V. et al 2012 *Phys. Plasmas* **19** 082504
- [19] Soukhanovskii V. et al 2013 *J. Nucl. Mater.* **438** S96
- [20] Soukhanovskii V.A. et al 2016 *IEEE Trans. Plasma Sci.* **44** 3445
- [21] Allen S.L. et al 2012 Results from initial snowflake divertor physics studies on DIII-D *Proc. 24th IAEA FEC—IAEA CN-197, (San Diego, 8–13 October 2012)* [PD/1-2] (www.naweb.iaea.org/napc/physics/FEC/FEC2012/html/proceedings.pdf)
- [22] Hill D. 2013 *Nucl. Fusion* **53** 104001
- [23] Soukhanovskii V. et al 2015 *J. Nucl. Mater.* **463** 1191
- [24] Calabro G. et al 2015 *Nucl. Fusion* **55** 083005
- [25] Greenwald M. et al 1988 *Nucl. Fusion* **28** 2199
- [26] Kolemen E. et al 2018 *Nucl. Fusion* submitted
- [27] Soukhanovskii V.A. et al 2014 Developing physics basis for the radiative snowflake divertor at DIII-D *Proc. 25th IAEA FEC—IAEA CN-221, (St. Petersburg, 16–21 October 2014)* [EX/7-4] (www.naweb.iaea.org/napc/physics/FEC/FEC2014/fec_sourcebook_online.pdf)
- [28] Soukhanovskii V.A. et al 2016 Snowflake divertor configuration effects on pedestal stability and edge localized modes in NSTX and DIII-D tokamaks *Preprint: 2016 IAEA FEC (Kyoto, Japan)* [EX/3-24] (www-pub.iaea.org/iaameetings/48315/26th-IAEA-Fusion-Energy-Conference)
- [29] Lasnier C. et al 2011 *J. Nucl. Mater.* **415** S353
- [30] Makowski M.A. et al 2012 *Phys. Plasmas* **19** 056122
- [31] Asakura N. et al 2013 *Fusion Sci. Technol.* **63** 70
- [32] Luo Z., Xiao B., Guo Y. and Ye M. 2014 *IEEE Trans. Plasma Sci.* **42** 1021
- [33] Petrie T. et al 2014 *J. Nucl. Mater.* **463** 1225
- [34] Ryutov D. et al 2012 Theory and simulations of ELM control with a snowflake divertor *Proc. 24th IAEA FEC—IAEA CN-197 (San Diego, 8–13 October 2012)* [TH/P4-18] (<http://naweb.iaea.org/napc/physics/FEC/FEC2012/html/proceedings.pdf>)
- [35] Ryutov D., Cohen R., Rognlien T. and Umansky M. 2012 *Contrib. Plasma Phys.* **52** 539
- [36] Umansky M.V. and Ryutov D.D. 2016 *Phys. Plasmas* **23** 030701
- [37] Canal G. et al 2015 *Nucl. Fusion* **55** 123023
- [38] Farmer W. and Ryutov D. 2013 *Phys. Plasmas* **20** 092117
- [39] Farmer W. 2014 *Phys. Plasmas* **21** 042114
- [40] Carlstrom T., Foote J., Nilson D. and Rice B. 1995 *Rev. Sci. Instrum.* **66** 493
- [41] Carlstrom T., Hsieh C., Stockdale R., Nilson D. and Hill D. 1997 *Rev. Sci. Instrum.* **68** 1195
- [42] Mclean A. et al 2015 *J. Nucl. Mater.* **463** 533
- [43] Umansky M., Rognlien T., Ryutov D. and Snyder P. 2010 *Contrib. Plasma Phys.* **50** 350
- [44] Eich T. et al 2011 *Phys. Rev. Lett.* **107** 215001
- [45] Goldston R. 2012 *Nucl. Fusion* **52** 013009
- [46] Scarabosio A. et al 2015 *J. Nucl. Mater.* **463** 49
- [47] Petrie T. et al 1997 *Nucl. Fusion* **37** 321
- [48] Fenstermacher M.E. et al 1999 *Plasma Phys. Control. Fusion* **41** A345
- [49] Leonard A., Makowski M., Mclean A., Osborne T. and Snyder P. 2015 *J. Nucl. Mater.* **463** 519
- [50] Petrie T. et al 2007 *J. Nucl. Mater.* **363–5** 416
- [51] Leonard A., Meyer W., Geer B., Behne D. and Hill D. 1995 *Rev. Sci. Instrum.* **66** 664
- [52] Lunt T. et al 2016 *Plasma Phys. Control. Fusion* **58** 045027
- [53] Reimerdes H. et al 2015 *J. Nucl. Mater.* **463** 1196